Geochemistry and oxygen isotope composition of magnetite from the Zhangmatun deposit, North China Craton: Implications for the magmatic-hydrothermal evolution of Cornwall-type iron mineralization

Qiuhong Xie [a], Zhaochong Zhang [a,*], Tong Hou [a], Ziliang Jin [a], M. Santosh [a,b]

[a] State Key Laboratory of Geological Process and Mineral Resources, China University of Geosciences, Beijing 100083, China
[b] Department of Earth Sciences, University of Adelaide, Adelaide, SA 5005, Australia

ABSTRACT

The Zhangmatun deposit is a high-grade skarn-type iron deposit genetically linked with a gabbroic intrusion, and it has been recognized as a typical example of "Cornwall-type" deposits in China. Electron microprobe (EMPA) and laser ablation-inductively coupled plasma-mass spectrometry (LA-ICP-MS) data on magnetite show decreasing contents of Ti, V, Cr, Mn, Co and Ga, from the gabbro, through the skarn, and to the iron ores. Additionally, magnetite grains from the gabbro, skarn and iron ores have similar primary mantle normalized signature and chondrite-normalized REE pattern, suggesting that the Fe in them might have be derived from a common source. The $\delta^{18}O_{V\text{-}SMOW}$ values of magnetite from iron ores mainly range from 4.3‰ to 6.4‰, markedly higher than that of magmatic magnetite (3.0‰). The significantly elevated oxygen isotopes of both magnetite and the corresponding water in the hydrothermal system are considered to reflect oxygen isotopic exchange between the ore-forming fluids and ^{18}O-rich carbonate rocks at relatively high temperature. Thus, the magnetite in the iron ores is inferred to be predominantly precipitated from the modified ore-forming fluids, rather than directly from the unreacted primary magmatic fluids. In the time-resolved analytical signals of LA-ICP-MS, the abnormal signals of incompatible elements such as Si, Ca and Mg are attributed to the sub-microscopic silicate mineral relicts. The inference is also supported by the BSE images and chemical maps of representative magnetite. The abnormal signals of Na and K are possibly related to the micro- to nano-scale salt-bearing fluid inclusions in magnetite. Based on the geochemical characteristics of different magnetite grains and varying FeO^T in the fresh and altered gabbroic rocks, we propose that the iron in the ores was mainly derived from leaching of the solidified ore-related gabbro during the contact metasomatism by hydrothermal fluids. The interaction between hydrothermal fluids and carbonate country rocks and the evolution of the ore-forming fluids, including the changes in geochemical composition, decreasing temperature and pressure, and increasing oxygen fugacity, provided the conditions for precipitation of magnetite from ore-forming fluids. Our study has potential implications in understanding the origin of 'Cornwall-type' deposits elsewhere world.

1. Introduction

Skarn-type iron deposits are mainly associated with intermediate-felsic igneous rocks, with only a small proportion related to mafic intrusions (Meinert, 1992; Meinert et al., 2005; Zhang et al., 2014b). The skarn-type iron deposits related to mafic intrusions are recognized as "Cornwall-type" deposits, based on the typical example of the deposit at Cornwall, Pennsylvania. Previous workers have demonstrated that the "Cornwall-type"

deposits are formed by metasomatic replacement (Eugster and Chou, 1979; Rose et al., 1985) and that the ore-forming fluids are spatially and temporally connected with mafic intrusions (e.g., Eugster and Chou, 1979). However, the source of iron still remains controversial. Among the various models proposed for the source of metallic iron are: 1) leaching from the high Fe-content mafic rocks (Lapham and Gray, 1973; Eugster and Chou, 1979); 2) exsolved Fe-rich fluids from the magma (Shimazaki, 1980); and 3) host sedimentary rocks (e.g., Triassic red beds, Rose et al., 1985) or pre-existing iron deposits (e.g., BIFs, Johnson et al., 1990).

In China, the skarn-type iron deposits are mainly distributed in the eastern part, including many large ore clusters such as those in

the Handan-Xingtai area of Hebei Province, Laiwu and Jinling of Shandong Province, Linfen area of Shanxi Province and Daye area of Hubei Province (Fig. 1a). The major skarn-type iron deposits in the North China Craton (NCC) are generally genetically related to dioritic intrusions, with an exception of the Zhangmatun high-grade iron deposit located in Ji'nan City, western Shandong Province, southeastern NCC which occurred at the contact zone between the Ji'nan gabbroic intrusion and carbonate rocks. This deposit is considered as a typical example of "Cornwall-type", a category which is rarely investigated in China except for the Cihai iron deposit found in Beishan region, Xinjiang (Hou et al., 2013; Tang et al., 2017; Zheng et al., 2017).

Magnetite is a common accessory mineral in magmatic, sedimentary, and metamorphic rocks (Ramdohr, 1980; Scheka et al., 1980; Dupuis and Beaudoin, 2011; Yang et al., 2000), and it is also a major or minor mineral in a range of mineral deposit types (Dupuis and Beaudoin, 2011). In recent years, several investigations have employed LA-ICP-MS to detect ppm to sub-ppm trace element concentrations in magnetite for tracing the genetic history (Dare et al., 2012; Nadoll and Koenig, 2011; Nadoll et al., 2014; Savard et al., 2010). Magnetite is also resistant to mechanical breakdown and chemical alteration and therefore the geochemistry of magnetite can preserve the primary composition and record significant information about the environment of formation (Grigsby, 1990; Meinert et al., 2005). The recent interest in the application of trace element signature of magnetite as provenance indicators, both in the exploration of ore deposits (Dupuis and Beaudoin, 2011; Nadoll et al., 2014) and in sedimentology (Grigsby, 1990; Razjigaeva and Naumova, 1992; Yang et al., 2009) is a testimony to the importance of this mineral as a proxy to determine provenance, and to understand the process of mineralization (Dare et al., 2012).

In this paper, we report the geochemical and oxygen isotopic composition of magnetite from iron ores, skarn (referred to endo-skarn in this paper) and the ore-related Ji'nan gabbroic intrusion. We use the data to trace the sources of iron, and offer some critical constraints on the genesis of "Cornwall-type" deposits.

2. Geological background

2.1. Regional geology

The West Shandong Province in the southeastern part of the NCC is bound to the east by the Tan-Lu fault zone, and to the south by Dabie-Sulu ultra-high pressure belt (Fig. 1a). The basement rocks in the regions are composed mainly of Neoarchean
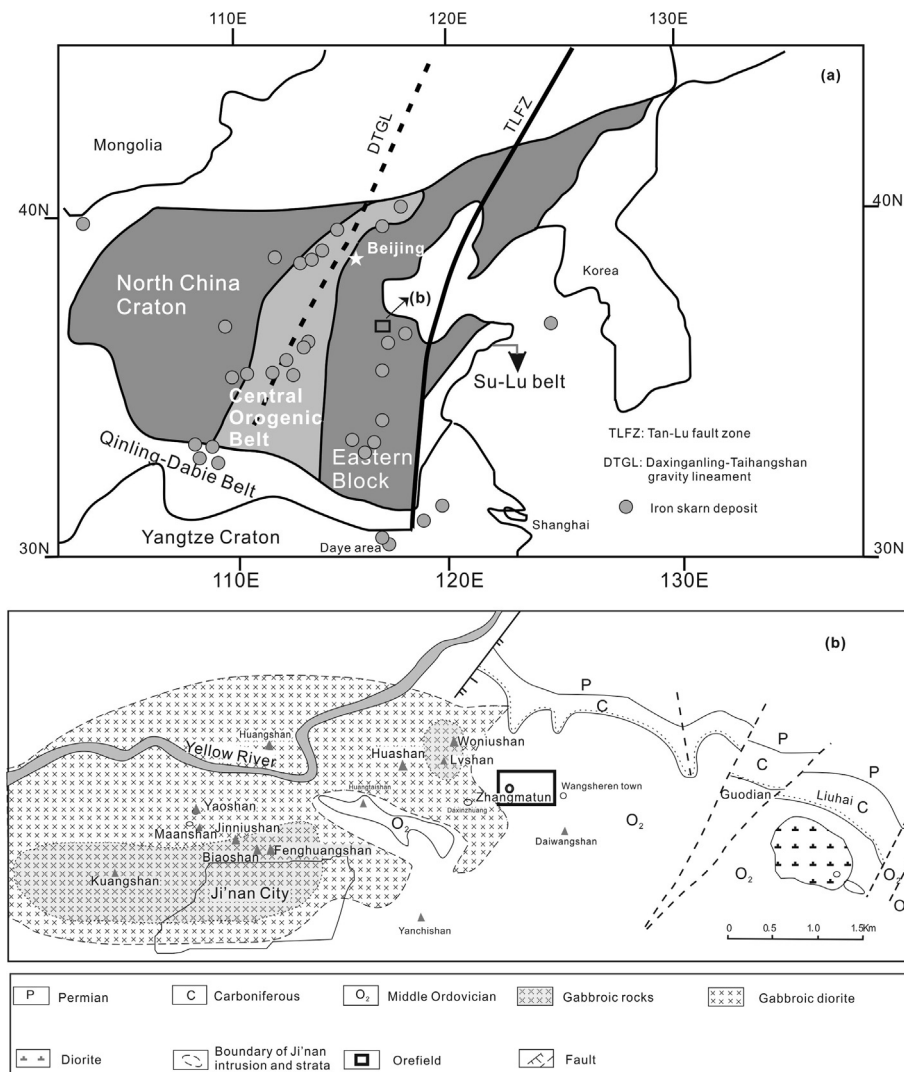

Fig. 1. (a) Simplified tectonic map of eastern China (modified from Xu (2002)), showing the locations of major skarn iron deposits in the North China Craton (after Zhang et al. (2014b), (b) Geological sketch of the Jinan mafic intrusion (modified from RGS (1991)).

medium-grade metamorphic rocks including biotite-gneiss, amphibolite, biotite-granulite, migmatite and migmatitic granite (Qiu et al., 2005; Yang et al., 2005), unconformably overlain by Precambrian-Ordovician marine carbonates and shales, Carboniferous-Permian terrestrial clastic rocks and Mesozoic sedimentary rocks (Liu et al., 2008). The Ji'nan area is cut through by the Juye-Liangshan-Ji'nan-Zibo ring fault belt (Song and Li, 2001; Zhang et al., 2007) and several small-scale NEE- or NNW-striking faults. Early Cretaceous magmatic rocks are widespread in the region, including the Ji'nan intrusion.

2.2. Deposit geology

The exposed strata in the Zhangmatun orefield mainly consists of the Cambrian Chaomidian and Gushan formations, lower Ordovician Sanshanzi Formation, middle Ordovician Majiagou Formation, and the overlying Mesozoic sedimentary rocks and Cenozoic fluvial and lacustrine sediments. The Majiagou Formation is predominantly composed of limestone/marble. NNW-striking faults and two groups of post-depositional fractures cut through the ore bodies.

The Ji'nan mafic intrusion was emplaced within the carbonate strata of the Middle Ordovician Majiagou Formation, and locally cut across Permian to Cretaceous strata (Fig. 1b). It is the largest pluton in the Ji'nan area, and mainly consists of gabbro showing compositional zoning from olivine-gabbro and gabbro in the center, gabbro in the transitional zone, to gabbro and gabbroic diorite in the marginal zone (RGS, 1991). The contact relationships between these phases are obscure (Fig. 1b). Most part of the Ji'nan intrusion in the Zhangmatun orefield is covered by the Quaternary sediments. However, samples from drill holes show that the ore-related igneous rocks beneath the orefield are gabbro in the marginal zone.

2.2.1. Iron orebodies

The Zhangmatun iron deposit is located in northeast Ji'nan city, West Shandong Block. It is a medium-sized high-grade skarn-type iron deposit. According to JiGang Co. Ltd., the resource of this iron deposit is about 20.47 Mt with an average Fe grade of ~52.25 wt% (up to 61.35 wt%).

The iron orebodies occur in the contact zone between the eastern marginal part of Ji'nan intrusion and the carbonate strata of the Ordovician Majiagou Formation (Fig. 1b). There are two deeply buried iron orebodies (the No. 1 and the No. 2) in the orefield. The No. 1 orebody is the predominant one, and is lenticular, 550 m long, 600 m deep, 1.52–70.73 m (21.68 m on average) thick, and steeply dipping at depth and gently dipping in the shallow section. The No. 2 orebody is also lenticular in shape and about 460 m in length, 230 m in depth, with thickness ranging from 1.35 m to 44.43 m (average 26.59 m).

The ore minerals of the Zhangmatun iron deposit are mainly subhedral granular magnetite (Fig. 2b), minor euhedral-subhedral pyrite and chalcopyrite. Massive magnetite ores are dominant, together with some densely disseminated iron ores (Fig. 2a, b). The gangue minerals are clinopyroxene, tremolite, phlogopite, serpentine, chlorite and calcite (Fig. 2c, d, h).

2.2.2. Hydrothermal alteration

From the sedimentary host rocks, through skarn to the ore-related gabbro, four main alteration zones have been identified: (1) Marble or re-crystallized carbonate zone formed from the Ordovician Majiagou limestone, where the genetically linked gabbro was emplaced. (2) Magnetite zone, the magnetite orebodies which show sharp contact with the carbonate zone. (3) Skarn alteration zone composed of typical skarn minerals such as diopside, and subordinate tremolite, albite, mica, chlorite, as well as magnetite, pyrite, chalcopyrite. (4) Na-alteration zone where albitization is generally observed (Fig. 2c) in the margin of the intrusion near the contact zone with the skarn, suggesting post-magmatic hydrothermal processes.

Four stages of mineralization have been recognized based on detailed petrographic observations as follows: (1) Prograde stage: biotite and amphibole replaced by diopside and albite (Fig. 2e–g). (2) Retrograde stage: in this stage, Fe-poor epidote, chlorite and amphibole (tremolite) replaced the diopside, and this stage was characterized by the precipitation of magnetite from the ore-forming fluids which resulted in the formation of massive iron ores. (3) Sulfide stage: pyrite and chalcopyrite replaced the magnetite in ores with the formation of chlorite, calcite and quartz. (4) Supergene stage: quartz and calcite were precipitated in this stage. These four stages represent decreasing temperature (Zheng et al., 2007).

3. Analytical methods

Polished thin sections of Ji'nan igneous rocks, (endo-) skarn and iron ores were used for petrographic studies. Geochemical compositions of the different magnetite grains were analyzed by electron microprobe analysis (EMPA) and laser ablation inductively coupled plasma mass spectrometry (LA-ICP-MS), and element contents of biotite and amphibole were obtained using EMPA. Magnetite grains separated from the Ji'nan gabbro and iron ores were used for oxygen isotopic analysis.

3.1. Mineral chemistry

EMPA of magnetite was carried out by using JEOL JXA-8230 at the Institute of Mineral Resources, Chinese Academy of Geological Sciences, while the measurement on several biotite and amphibole were performed by wavelength dispersive analysis (WDP) using standard procedures on the EPMA-1600 Superprobe at the State Key Laboratory of Geological Process and Mineral Resources of the China University of Geosciences, Beijing. The analyses above were under the same operating conditions with an acceleration voltage of 15 kV, a beam current of 20 nA and 1–5 μm beam diameter. The measured data were corrected using ZAF correction procedure after Armstrong (1995) and the precision is better than 1 wt% (Jin et al., 2014). Additionally, during the process of EMPA of magnetite, some representative grains are mapped in detail using electro microprobe.

The in-situ LA-ICP-MS of magnetite grains in the thin sections of different rocks were carried out at National Research Center for Geoanalysis, Chinese Academy of Geological Sciences. Trace elements of magnetite were determined by a New Wave UP 213 Nd:YAG Laser Ablation system coupled with a Thermo Element II ICP-MS. Helium was applied as a carrier gas, while argon was used as makeup gas and mixed with the helium via a T-connector before entering the ICP. Each analysis was performed by a laser spot of 40 μm in diameter with successive pulses at 10 Hz. Each analysis includes a background acquisition of approximately 20 s for gas blank, followed by data acquisition of 40 s from the sample. The external reference material NIST-612 (Duan et al., 2012) was used to calibrate element concentrations and ^{57}Fe was used as internal standard (Gao et al., 2013; Chen et al., 2015). In addition, major element contents (i.e., Fe) of magnetite by LA-ICP-MS were corrected with the results of EMPA.
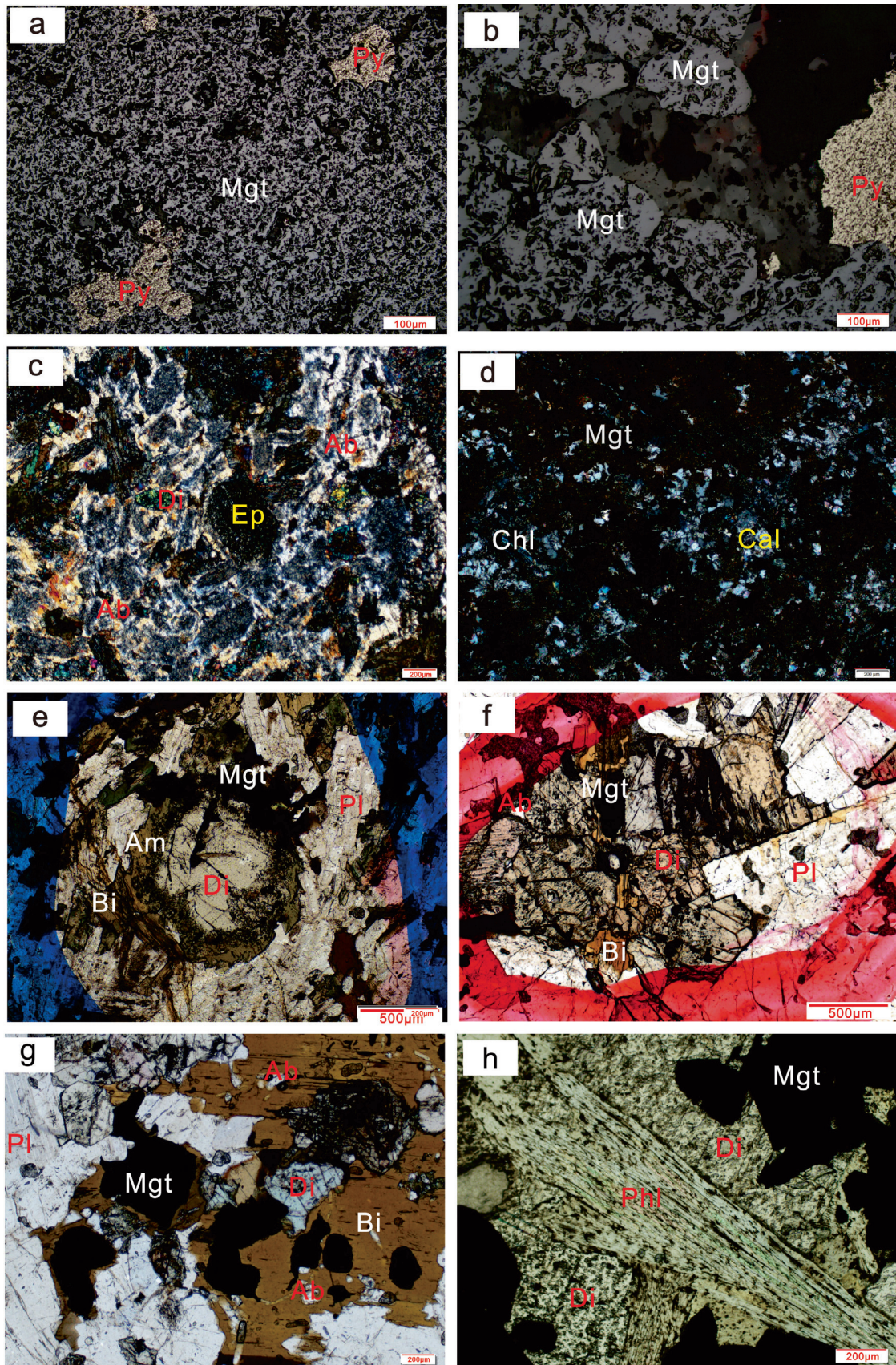
Fig. 2. Photomicrographs of iron ore and albitized gabbroic rocks. (a) Massive iron ore (reflected light), (b) Subhedral-anhedral grainy magnetite (reflected light), (c) Strongly albitized gabbro in the orefield (cross-polarized light). (d) Gangue minerals, such as chlorite, calcite in the orefield (cross-polarized light), (e) Biotite and amphibole altered into diopside, albite and magnetite (plane-polarized light), (f, g) Biotite replaced by diopside, along with the newly forming of magnetie (plane-polarized light), (h) Phlogopite growing with diopside and magnetite (plane-polarized light). Abbreviations: Mgt-magnetite, Py-pyrite, Di-diopside, Ep-epidote, Ab-albite, Chl-chlorite, Cal-calcite, Am-amphibole, Bi-biotite, Pl-plagioclase, Phl-phlogopite.

3.2. Oxygen isotope

Single magnetite grains were separated under a binocular microscope. The BrF_5 method was used in preparation for oxygen isotope samples. Oxygen from magnetite was liberated by reaction with BrF_5 in nickel reaction vessel at ∼550 °C. The O_2 was converted into CO_2 by reaction with kryptol at 700 °C, following by collection into a sample tube for mass-spectrometric analysis of oxygen isotope. Measurement of oxygen isotope ratios was performed using a MAT-253 mass spectrometer at the Institute of Mineral Resources, Chinese Academy of Geological Sciences. The oxygen isotopic compositions are reported in the conventional δ notation relative to SMOW. The external precision of $δ^{18}O$ was 0.2‰ (1SD), based on repeated measurements of standard samples. Detailed processes have been described by Li et al. (2014).

4. Results

4.1. Mineral chemistry

The chemical compositions of representative biotite and amphibole grains are presented in Table 1, and those of magnetite analyzed by EMPA are listed in Table 2. The BSE images and the chemical maps of magnetite are presented in Fig. 3, and the analytical results of magnetite by LA-ICP-MS are given in Tables 3 and 4. Trace element concentrations of magnetite discussed in this paper are mainly based on the data in Tables 3 and 4 because of the more reliability of LA-ICP-MS. However, concentrations of Fe in magnetite are based on data presented in Table 2.

All the magnetite grains have substantial Ti (2450–56858 ppm in magnetite from Ji'nan intrusion, 244–1051 ppm

Table 1
Representative analyses of biotite and amphibole from the ore-related gabbro (by EMPA).

Mineral	Sample	SiO$_2$	TiO$_2$	Al$_2$O$_3$	Fe$_2$O$_3$	FeO	MnO	MgO	CaO	Na$_2$O	K$_2$O	Total
Biotite	JN-26-1	37.67	2.37	13.53	0	11.98	0.04	18.87	0	0.42	9.22	94.1
	JN-28-1	37.4	2.78	13.12	0	12.86	0	19.64	0.06	0.27	7.93	94.06
	JN-D-1-4	35.11	5.06	13.5	0	18.61	0.11	13.3	0.08	0.5	8.63	94.9
	JN-30-4	35.5	3.84	13.13	0	19.96	0.08	12.29	0.13	0.28	9.26	94.47
Amphibole	JN-35-1	41.60	2.09	11.73	0	10.82	0.06	15.43	11.23	3.36	0.83	97.15
	JN-30-2	49.52	0.84	4.64	0	15.76	0.39	14.18	10.62	1.01	0.39	97.35

Table 2
Representative analyses of magnetite from Ji'nan intrusion, skarn and iron ores by EMPA.

| Host rock	Sample	SiO$_2$	TiO$_2$	Al$_2$O$_3$	FeO	MnO	MgO	CaO	Na$_2$O	K$_2$O	P$_2$O$_5$	Cr$_2$O$_3$	V$_2$O$_3$	Cl	Total
		wt%													
Ji'nan intrusion	YS-3-2-5	0.04	0.78	0.54	88.89	0	0.03	0	0	0	0	0.81	1.90	0	92.98
	YS-2-2	0.03	3.84	5.64	80.47	0.54	0.40	0	0.21	0.01	0.03	0.07	0.82	0	92.07
	KS-1-1	0	1.54	1.21	88.32	0.07	0.11	0	0.05	0.01	0	1.35	1.72	0.01	94.39
	KS-1-2	0.03	2.07	1.53	87.87	0.08	0.15	0	0	0	0	1.21	1.64	0	94.58
	FH-2-1	0.06	4.92	3.03	83.71	0.28	1.06	0	0.03	0.02	0	0.67	1.25	0	95.03
	FH-2-3	0.01	4.71	2.53	84.60	0.21	0.92	0	0.03	0.01	0	0.60	1.26	0.01	94.88
	BS-3-1	0	7.85	3.13	81.21	0.29	0.83	0	0.03	0.01	0.02	0.40	1.38	0	95.15
	BS-3-2	0.05	10.77	3.07	79.22	0.34	1.25	0	0.04	0	0	0.32	1.16	0.01	96.24
	KS-2-1	0.01	6.61	3.46	81.77	0.20	0.86	0	0	0	0.02	0.93	1.65	0	95.52
	KS-2-2	0.07	7.47	3.28	81.43	0.26	0.91	0	0	0	0	0.78	1.66	0.01	95.86
	KS-2-3	0.08	7.54	3.33	81.34	0.22	0.86	0	0	0	0.04	0.86	1.56	0	95.82
	YS-1-1	0.77	8.85	0.52	80.25	0.08	0.26	0.07	0.02	0	0.02	0.42	1.06	0	92.33
	YS-1-3	0	3.51	2.16	83.80	0.18	0.44	0.08	0	0	0	0.72	1.64	0.01	92.53
	ZMT-11-1	0.07	0.36	0.09	92.44	0.03	0	0	0	0	0	0.14	1.06	0	94.18
	ZMT-11-2	0.11	0.44	0.03	92.58	0.04	0	0	0.04	0.01	0	0.05	0.60	0	93.89
	ZMT-15-2	0.01	6.56	3.29	81.23	0.45	0.36	0	0.02	0	0	0.23	0.88	0	93.03
Skarn	ZMT-10-1	0.09	0.92	0.71	91.41	0.10	0.04	0	0	0	0	0.19	0.62	0	94.09
	JN-5'-1	0.06	0.18	0	91.34	0.09	0.68	0	0	0	0	0.02	0.06	0.01	92.42
	JN-5'-2	0.06	0.14	0.02	92.41	0.05	0.66	0	0.04	0	0	0.01	0.07	0	93.44
	JN-10-4-1	2.81	0.18	0.52	83.86	0.03	0.55	0.43	0.13	0.08	0.01	0.04	0.25	0	88.89
	JN-5-1	0.07	0.03	0	90.31	0.08	0.56	0	0.02	0	0	0.04	0.02	0	91.14
	JN-5-2	0.02	0.11	0.03	89.30	0	0.57	0	0	0	0.04	0.02	0.02	0.02	90.12
	JN-10-3-1	1.11	0.10	0.10	88.06	0	0.11	0.05	0.09	0	0	0.01	0.04	0.01	89.66
	JN-10-3-2	0.08	0.02	0	86.67	0.03	0	0.21	0	0.01	0	0	0.23	0.01	87.25
	JN-10-3-3	1.29	0.04	0.15	87.60	0	0.20	0.10	0.01	0.03	0.02	0.02	0.09	0.01	89.55
	JN-10-1-1	3.70	0.20	0.76	82.82	0.03	0.85	0.98	0.11	0.12	0.02	0.04	0.15	0.03	89.81
	JN-10-1-2	2.22	0.22	1.47	84.63	0.06	0.36	0.16	0.24	0.05	0	0.08	0.09	0.01	89.57
Iron ores	JN-4-1	1.04	0.03	0.40	86.27	0.16	3.09	0.19	0.04	0.01	0.04	0.02	0.08	0.01	91.36
	JN-4-2	0.02	0.04	0.35	86.34	0.11	2.84	0	0.02	0	0	0.03	0.04	0.02	89.79
	JN-6-1	0.03	0.04	0.31	88.99	0.13	1.49	0	0.02	0	0.01	0	0.07	0.02	91.10
	JN-13-1	0.27	0.09	0.48	88.23	0.23	2.59	0.02	0.04	0.01	0	0.02	0.03	0.02	92.00
	JN-15-1	0.02	0.00	0.16	91.55	0	0.29	0	0.01	0	0	0.02	0.01	0	92.06
	JN-15-2	0.14	0.00	0.10	91.68	0	0.17	0	0.02	0	0.03	0.01	0.01	0	92.16
	JN-16-1	0.72	0.07	0.48	89.45	0	0.42	0.06	0.01	0.04	0.03	0.03	0.02	0.01	91.32
	JN-16-2	1.37	0.18	0.25	89.29	0	0.44	0.05	0.08	0.08	0.01	0.02	0.04	0.01	91.82
	JN-8-1	0	0.06	0.20	90.33	0.12	2.36	0	0	0.01	0.04	0.06	0.07	0	93.24
	JN-8-2	0	0.01	0.44	88.63	0.14	2.40	0	0.03	0	0	0.02	0.08	0.02	91.77
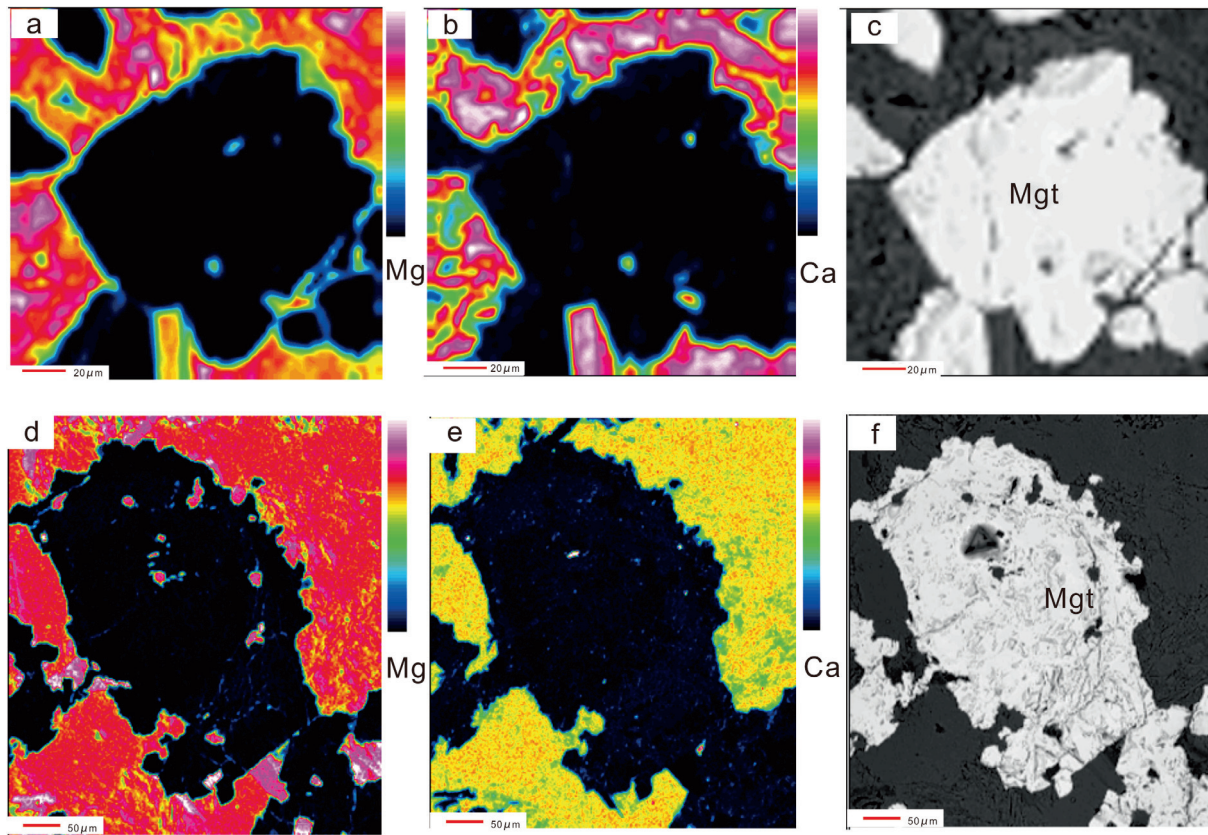
Fig. 3. BSE images (c and f) and chemical maps (a, b and d, e) of representative magnetite grains, (a), (b), (c) for one grain while (d), (e), (f) for another.

in magnetite from skarn, and 8–604 ppm in magnetite from iron ores), V (5345–10,753 ppm in magnetite from Ji'nan intrusion, 69–1684 ppm in magnetite from skarn, and ≤522 ppm in magnetite from iron ores), Al (1322–24,420 ppm in magnetite from Ji'nan intrusion, 49–4966 ppm in magnetite from skarn, and 266–8090 ppm in magnetite from iron ores), Mn (516–5788 ppm in magnetite from Ji'nan intrusion, 191–668 ppm in magnetite from skarn, and 122–2071 ppm in magnetite from iron ores), Si, Zn, Co, and Ga. Cr (315–5582 ppm in magnetite from Ji'nan intrusion, ≤55 ppm in magnetite from skarn, and ≤29 ppm in magnetite from iron ores) is only enriched in magnetite from igneous rocks while Ca (≤3228 ppm in magnetite from Ji'nan intrusion, 78–4719 ppm in magnetite from skarn, and 105–70,520 ppm in magnetite from iron ores) is mainly contained in magnetite from skarn and ores. The data show decreasing trends of concentrations of Ti, V, Cr, Mn, Co and Ga concentrations in magnetite from the ore-related intrusion, through the skarn, to iron ores. Traces of Na and K (Table 3) were also detected in some magnetite grains.

Considering that the concentrations of some trace elements of magnetite are below the detection limits, we take the average compositions to compare different types of magnetite grains. As shown in Fig. 4, the magnetite grains from three types of host rocks exhibit similar features in primitive mantle normalized spidergrams (Fig. 4a) and chondrite-normalized REE patterns (Fig. 4b). However, compared with the skarn and iron ores, magnetite from the Ji'nan intrusion is characterized by higher enrichment of compatible elements such as V, Ti, Cr, Mn, Zn, Ni and Ga, and more depletion in incompatible elements such as Si, Al, Ca, Ba, Sr, U and Th. In addition, the REE concentrations of magnetite from the Ji'nan intrusion are much lower than those from skarn and iron ores.

4.2. Oxygen isotope systematics

Table 5 shows $\delta^{18}O_{V-SMOW}$ value of 3.0‰ for magnetite from the ore-related gabbro beneath the Zhangmatun orefield. The data is consistent with the oxygen isotopic compositions ($\delta^{18}O_{V-SMOW}$ = 1.64–4.16‰) of magnetite from the Ji'nan intrusion reported by Yang et al. (2012). Magnetite from iron ores has $\delta^{18}O_{V-SMOW}$ values ranging from 4.3‰ to 6.4‰, which are markedly higher than that of the Ji'nan magmatic intrusion. However, the sample JN-7 from iron ores shows a much lower value of 2.5‰, which might reflect the contamination of ^{18}O-poor minerals adjoined to the magnetite.

5. Discussion

5.1. Effect of inclusions

Magnetite is one of the most common oxide minerals of the spinel group, with an inverse spinel structure and general stoichiometry of AB_2O_4 (Bragg, 1915; Fleet, 1981, 1986; Nadoll et al., 2014), where A presents a divalent cation such as Fe^{2+}, Mn, Mg, Zn, Ni or Co, B presents a trivalent cation such as Al, Fe^{3+}, Cr, V, Mn or Ga (Nadoll et al., 2014; Dupuis and Beaudoin, 2011). Titanium with a 4+ charge can also occupy the B site when substitution is coupled with a divalent cation (Wechsler et al., 1984). All the elements above are compatible in magnetite with concentrations above the detection limits. However, in our study, many highly incompatible trace elements such as Si, Ba, Sr, Ca, Na and K are also detected in some magnetite. Although the weak fraction of elements under magmatic condition, and/or the possible relatively elevated partition coefficients of incompatible trace elements under

Table 3
Representative trace element concentrations of magnetite from Ji'nan intrusion, skarn and iron ores by LA-ICP-MS.

Host rock	Sample no.	Si	Ba	Sr	U	Th	Ca	Pb	Al	Nb	Sn	Ga	Mn	Mg	Ti	Zn	Co	V	Ni	Cr
		ppm																		
Ji'nan intrusion	KS-1-1	5334	3	5	0	–	353	0	15,490	1	9	106	1762	4523	32,521	1243	317	5781	592	5364
	KS-1-2	1194	1	1	0	–	210	0	16,216	0	7	101	2047	3972	37,622	1496	344	5647	588	5582
	KS-1-3	708	0	0	–	–	0	0	14,155	0	9	134	2067	3439	38,845	1644	306	7611	505	5229
	FH-2-2	868	–	0	0	–	15	–	17,889	0	8	107	1840	4632	30,619	1645	248	5590	371	3430
	FH-2-3	1371	–	1	–	–	451	0	18,732	0	8	148	2178	5401	32,744	1345	270	7549	396	3848
	BS-3-1	4145	13	34	0	0	2628	0	24,420	1	7	99	2418	6304	45,335	1407	261	7122	412	2729
	BS-3-2	773	0	1	0	0	175	0	17,047	2	9	120	2054	3880	43,243	1687	259	7965	350	2709
	BS-3-3	193	–	–	0	–	23	–	17,668	1	8	121	2263	5232	48,562	1541	248	7059	288	2052
	KS-2-1	1125	–	0	–	–	33	–	16,718	0	7	117	2224	5483	47,720	1679	295	10,709	505	4904
	KS-2-2	876	1	0	–	–	0	0	13,049	5	7	105	2420	3092	56,450	1428	272	9169	364	4847
	KS-2-3	924	1	0	–	–	80	–	13,101	0	6	121	2686	4337	56,858	1807	300	10,753	485	4667
	YS-3-2-1	0	–	–	0	0	0	0	3445	–	5	103	1222	237	4108	298	93	5643	116	1958
	YS-3-2-2	0	–	–	–	–	93	0	3570	0	7	135	967	252	2948	297	108	7116	160	2171
	YS-3-2-3	37	–	–	–	0	22	0	3279	0	8	138	926	238	2675	590	108	7437	141	2191
	YS-2-1	646	–	–	0	–	0	0	2227	0	7	128	673	269	3280	831	116	6969	184	364
	YS-2-3	583	–	–	0	0	12	0	1918	0	9	137	516	224	2450	893	126	7313	211	315
	ZMT-11-1	1077	0	7	0	1	3228	0	2030	0	4	102	1851	261	9484	717	74	5345	54	1196
	ZMT-11-3	959	–	1	0	0	959	0	2294	0	4	107	835	148	4613	861	71	6110	57	849
	ZMT-11-4	822	–	0	0	0	20	3	1322	8	1	93	5788	330	53,379	445	68	5639	25	1497
	ZMT-15-1	625	0	0	0	0	50	–	4704	0	8	149	740	523	7970	1369	122	5836	217	950
Skarn	ZMT-10-1	1830	4	–	0	1	169	0	3329	11	9	144	1245	1000	33,122	1331	136	8052	210	1924
	ZMT-10-3	1029	0	0	0	–	0	0	3103	0	8	131	717	287	4565	856	113	6260	159	1719
	JN-10-3-1	9220	10	10	0	0	1304	5	1422	1	1	43	225	1700	737	42	30	580	326	13
	JN-10-3-2	28,727	312	287	1	0	3986	556	273	1	–	20	453	3904	244	36	942	1684	579	6
	JN-10-1-1	14,493	30	29	1	0	4519	0	4966	2	3	59	268	5280	724	35	35	263	316	1
	JN-10-4-1	5104	8	9	0	0	654	6	836	0	0	39	191	740	511	41	1	642	427	6
	JN-10-4-2	16,140	48	36	1	1	4611	1	3907	4	5	62	301	4609	1051	61	17	346	280	11
	JN-10-4-3	13,493	46	35	1	1	4719	2	2850	2	1	46	255	3458	926	54	2	578	393	0
	JN-5-1-1	1371	1	2	0	0	118	0	421	0	0	9	433	4336	1108	30	17	229	–	21
	JN-5-1-2	608	1	0	–	–	125	0	276	–	2	5	517	3898	1023	27	6	251	–	12
	JN-5-1-3	1233	0	0	–	0	118	0	125	0	0	2	647	4094	501	25	9	198	–	49
	JN-5-1-4	4315	0	0	0	0	202	0	890	0	0	1	628	7398	480	25	9	220	–	55
	JN-5-1	8396	0	2	0	0	202	–	117	2	0	2	668	11,029	394	24	11	69	19	0
	JN-5-2	2477	3	3	0	0	1701	0	252	1	2	2	615	5839	671	23	8	137	–	12
	JN-5-3	367	1	0	0	0	78	–	123	0	1	3	547	4078	692	25	6	249	–	39
	JN-5-4	3172	1	5	0	0	919	0	49	1	1	0	644	4843	485	23	10	77	7	2
Iron ores	JN-15-1	0	3	7	0	1	1110	0	3684	1	3	38	343	4284	380	24	80	28	56	–
	JN-15-2	0	1	3	0	0	178	0	758	0	3	33	243	877	117	22	76	44	29	4
	JN-15-3	334	5	4	0	0	105	0	266	0	0	23	241	546	91	27	74	212	473	3
	JN-4-1	4037	4	10	0	3	2121	0	4161	6	7	3	803	18,050	162	164	25	189	–	10
	JN-4-2	2646	0	2	0	0	336	0	3467	1	7	2	821	18,460	158	164	8	164	–	7
	JN-6-1	2246	4	9	0	0	929	0	7132	2	5	11	821	10,470	266	262	58	276	–	11
	JN-6-2	4833	3	14	0	0	1012	0	4902	2	4	10	861	14,315	292	79	25	267	–	7
	JN-6-3	2684	4	11	0	1	1524	0	6134	3	5	15	916	14,160	235	267	46	255	–	6
	JN-13-1	1445	2	6	0	0	1079	0	7126	0	3	11	2067	15,864	523	794	115	518	14	4
	JN-13-2	3511	24	14	0	0	533	1	7753	1	4	12	2063	17,520	474	653	102	522	–	7
	JN-13-3	1264	4	13	0	0	902	0	8090	1	7	14	2071	16,444	522	902	107	542	–	10
	JN-16-1	491	7	7	0	0	431	–	1502	0	1	25	122	1477	466	7	55	83	2	29
	JN-16-2	4209	23	29	0	0	1180	0	2255	1	1	44	123	3115	596	21	53	109	–	8
	JN-16-3	3654	12	26	0	0	997	0	2479	0	1	35	138	2725	604	20	53	68	–	9
	JN-8-1	1777	2	3	0	0	719	0	5833	0	5	12	1267	16,181	229	435	41	483	–	6
	JN-8-2	2497	5	5	0	0	375	0	4445	1	3	12	1251	15,654	253	299	55	471	–	8
	JN-8-3	944	9	50	0	0	70,520	0	0	0	2	0	1360	26,009	8	71	17	0	9	17

Note: "–" means element concentration below detected limit of IA-ICP-MS.

hydrothermal condition (Hu et al., 2014) might contribute to this feature, the irregular occurrences of Si, Ca, Na and K in magnetite indicates that they are not the controlling factors. Additionally,

many previous studies have demonstrated that magnetite always contains various sized inclusions which may represent relict of early minerals or fluids (Nadoll et al., 2014; Nadoll and Koenig,

Table 4
Representative rare earth element (REE) concentrations (in ppm) of magnetite from Ji'nan intrusion, skarn and iron ores by LA-ICP-MS.

Host rock	Sample	La	Ce	Pr	Nd	Sm	Eu	Gd	Tb	Dy	Ho	Er	Tm	Yb	Y	Lu
Ji'nan intrusion	KS-1-1	0.745	0.671	0.145	0.332	0.1	0.036	0.75	0.122	0.178	0.008	–	0.005	–	0.196	–
	KS-1-2	–	0.044	0.018	0.113	0.248	–	0.254	0.017	–	0.009	0.044	–	–	0.017	–
	KS-1-3	0.051	–	0.011	–	0.034	0.03	0.751	0.03	0.183	–	–	0.01	0.034	0.019	0.002
	FH-2-2	–	0.01	0.062	0.166	0.049	–	0.577	0.07	0.023	–	–	–	0.048	–	0.014
	FH-2-3	–	0.047	0.005	–	–	0.005	–	–	0.085	0.008	–	0.005	0.002	0.072	0.002
	BS-3-1	0.414	0.404	0.043	0.29	–	0.099	–	–	0.083	–	–	0.002	–	0.039	–
	BS-3-2	–	0.183	0.011	0.143	0.159	0.014	–	–	–	–	0.068	–	0.013	–	–
	BS-3-3	0.064	–	0.016	0.16	–	0.085	0.311	0.035	–	0.002	–	–	0.032	0.193	–
	KS-2-1	–	–	0.027	–	–	–	0.683	0.042	–	–	–	–	–	0.02	–
	KS-2-2	0.024	0.128	0.073	0.022	–	–	–	0.011	–	–	0.001	0.014	–	–	–
	KS-2-3	–	–	–	–	–	0.02	0.713	0.004	–	0.011	–	–	–	–	0.014
	YS-3-2-1	0.007	–	0.006 -	–	0.032		0.074	0.031	–	0.002	0.025	–	0.102	–	–
	YS-3-2-2	0.087	0.086	–	0.143	–	0.006	0.348	0.066	0.016	–	–	0.011	0.021	0.083	0.01
	YS-3-2-3	0.027	0.172	0.024	–	0.067	–	–	0.012	0.092	–	–	–	0.008	–	0.012
	YS-2-1	0.02	–	–	–	0.094	–	0.021	–	0.049	0.007	–	–	0.057	0.186	–
	YS-2-3	0.056	0.107	–	–	0.046	0.052	–	0.088	0.072	–	0.017	0.006	0.02	–	0.009
	ZMT-11-3	3.24	6.584	0.759	2.32	0.206	–	–	0.012	–	0.076	–	0.035	–	0.621	0.001
	ZMT-11-4	0.034	0.304	–	0.41	–	0.341	0.141	–	–	0.018	–	–	0.147	0.468	0.054
	ZMT-15-1	–	0.019	0.036	0.142	0.053	0.009	0.005	0.004	–	0.007	–	–	0.008	0.171	–
Skarn	ZMT-10-1	0.364	0.72	0.117	0.276	0.06	0.053	–	–	–	–	0.073	–	0.215	0.149	0.029
	ZMT-10-3	0.08	–	0.014	–	0.112	0.027	–	–	0.136	0.004	0.04	0.013	–	–	0.005
	JN-10-3-1	0.395	0.341	0.081	0.184	–	0.062	0.557	0.088	0.189	0.061	0.139	0.003	0.098	0.457	0.004
	JN-10-3-2	1.112	0.814	0.066	0.28	0.076	0.011	0.351	–	0.02	0.01	0.054	–	0.056	0.447	0.008
	JN-10-1-1	1.98	2.853	0.186	0.586	0.172	0.1	–	–	0.129	0.024	0.095	0.008	0.053	1.03	0.023
	JN-10-4-1	0.688	0.535	0.049	0.104	–	0.011	0.055	0.143	–	–	0.144	0.009	–	0.1	–
	JN-10-4-2	2.758	4.451	0.441	0.148	0.423	–	2.766	–	0.168	–	–	0.035	0.456	1.142	0.055
	JN-10-4-3	2.147	3.031	0.126	0.716	0.221	–	–	–	0.372	0.048	0.176	0.046	0.348	1.262	0.074
	JN-5-1-1	–	0.086	–	–	–	–	0.036	0.012	–	–	0.007	–	0.002	–	0.006 -
	JN-5-1-2	–	0.152	–	–	0.105	–	0.184	0.106	–	–	0.07	0.016	0.027	–	–
	JN-5-1-3	–	–	0.016	–	–	0.031	–	–	–	0.026	0.037 -	–	0.15	–	–
	JN-5-1-4	0.015	0.208	0.036	–	0.05	0.111	0.257	0.025	0.015	0.012	–	–	–	–	0.013
	JN-5-1	0.375	0.832	–	0.196	0.186	0.112	0.217	–	0.026	0.017	–	–	0.015	0.36	0.027
	JN-5-2	0.107	0.399	0.113	0.057	0.187	–	0.544	0.165	0.069	–	–	–	0.021	0.184	0.032
	JN-5-3	–	0.108	–	0.172	–	0.032	–	–	0.026	0.006	0.08	0	–	–	0.009
	JN-5-4	0.419	1.058	0.17	0.574	0.064	–	–	0.052	–	0.005	0.089	–	0.054	0.551	0.013
Iron ores	JN-15-1	1.641	2.141	0.207	0.802	0.179	0.042	0.207	–	0.579	0.055	0.241	0.072	0.294	2.684	0.06
	JN-15-2	0.223	0.21	0.051	0.009	0.033	–	–	–	0.088	0.003	–	0.013	0.054	0.446	0.013
	JN-15-3	0.147	0.315	0.014	0.141	–	–	–	0.055	0.037	0.013	0.097	0.001	0.021	0.129	0.014
	JN-4-1	1.926	4.096	0.621	3.132	0.622	0.103	0.485	0.15	0.491	0.057	0.102	0.014	0.093	2.906	0.036
	JN-4-2	0.201	0.148	0.04	–	0.08	–	–	–	0.083	0.014	–	0.013	0.093	0.179	0.023
	JN-6-1	0.192	0.463	0.114	–	–	0.103	0.59	0.011	–	–	0.115	0.001	0.023	0.369	–
	JN-6-2	0.338	1.438	0.059	0.381	0.134	0.012	–	–	0.116	0.021	0.095	0.012	–	0.499	0.015
	JN-6-3	0.906	1.721	0.171	0.86	0.449	–	–	–	0.245	0.018	0.05	0.006	0.108	0.692	0.022
	JN-13-1	0.255	–	–	0.336	0.06	0.065	–	0.055	–	0.028	0.118	0.013	–	–	0.013
	JN-13-2	0.089	0.341	0.011	–	–	–	1.136	–	–	0.001	0.062	0.011	0.018	0.198	0.022
	JN-13-3	0.246	0.352	0.084	0.248	–	0.033	0.417	–	0.109	0.025	–	–	0.118	0.174	–
	JN-16-1	0.6	0.276	0.024	–	0.094	–	0.01	0.069	0.008	0.027	–	–	–	0.137	0.012
	JN-16-2	0.549	1.241	0.083	0.382	0.344	–	–	–	0.094	0.02	0.049	–	–	0.513	–
	JN-16-3	0.226	0.583	–	0.393	0.162	0.057	0.208	0.032	0.047	–	0.036	0.003	–	0.357	0.005
	JN-8-1	–	0.17	0.004	–	0.015	–	–	–	–	–	0.02	0.009	0.017	0.088	0.006
	JN-8-2	0.132	0.078	–	0.162	0.037	0.033	–	0.086	0	0.003	–	0.003	–	0.052	0.016

Note: "–" means element concentration below detected limit of IA-ICP-MS.

2011; Huang et al., 2013). Because of the relatively large beam diameter, some micro and nano-scale inclusions might have been involved into the compositional analysis of magnetite during the analytical process by LA-ICP-MS, which may mask the true compositions of the pure magnetite (Zhao and Zhou, 2014). In general, inclusions exposed on the section surface can be observed under microscope, whereas the unexposed inclusions can be verified on the time-resolved analytical signals of LA-ICP-MS analyses.

Based on previous studies, Si and Ca are considered to enter magnetite structure along with a small proportion of Mg and Al (Bowles et al., 2011). However, as shown in Fig. 5, the poor correlation between Mg (and Al) and Si implies that Si may not partition as Mg and Al. Moreover, positive correlations between the typical outliers, i.e., Na and K, and Si indicate the similar states of these trace elements, suggesting that these may be mainly contained in inclusions.

Fig. 6 shows the time-resolved analytical signals of LA-ICP-MS analyses for some representative magnetite grains. Fig. 6a is from pure magnetite, exhibiting signals of the dominant elements (such as Fe, V, Ti, Cr, Mn, Ni and Co) and signals of incompatible trace elements consistent with those of the background. Fig. 6b shows signals of magnetite with inclusion and is characterized by the significant abnormalities of Si, Ca and Al in the interval of 50–65 s, suggesting the presence of sub-microscopic silicate mineral relict in magnetite. This is also supported by the BSE images and chemical maps (Fig. 3), which show that many small sized Mg-rich (and/or Ca-bearing) silicate minerals are contained in magnetite grains. In Fig. 6c, signals showing abnormalities of Na and K can be observed only in the interval of 20–45 s, which is generally attributed to salts in micro- to nano-scale fluid inclusions.
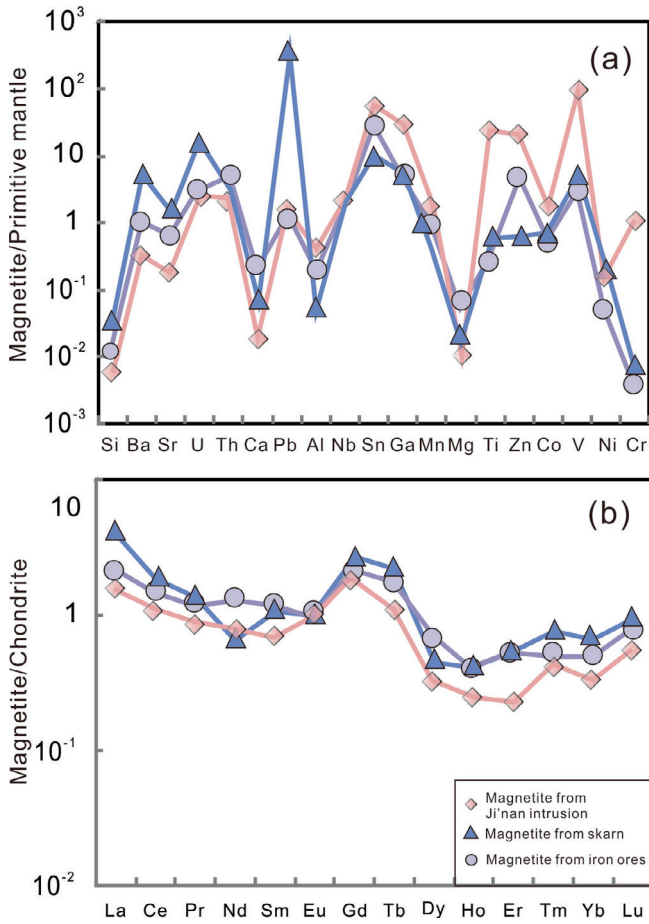
Fig. 4. (a) Primitive mantle-normalized spider-gram for magnetite from different rocks. Normalized values are from Han et al. (2002). (b) Chondrite-normalized rare element pattern of magnetite from different rocks. Normalization values are from Sun and McDonough (1989).

5.2. Implications for magmatic-hydrothermal evolution

As demonstrated by many studies over the last few decades, magnetite can form in a wide variety of different environments and its geochemical composition varies in response to varying

Table 5
Oxygen isotopic compositions of analyzed magnetite from the gabbro and iron ores.

Sample	Lithology	Mineral	$\delta^{18}O_{V\text{-}SMOW}$ ‰
JN-33	Gabbro	Magnetite	3.0
JN-4	Iron ore	Magnetite	4.5
JN-7	Iron ore	Magnetite	2.5
JN-8	Iron ore	Magnetite	5.4
JN-15	Iron ore	Magnetite	5.3
JN-16	Iron ore	Magnetite	5.7
JN-21	Iron ore	Magnetite	6.4
JN-22	Iron ore	Magnetite	5.3
JN-23	Iron ore	Magnetite	4.3

formation conditions (Beaudoin et al., 2007; Carew, 2004; Gosselin et al., 2006; Singoyi et al., 2006). The mineral is therefore widely used as a well-recognized petrogenetic indicator (Nadoll et al., 2014). In general, magnetite from intrusive rocks is controlled by the nature of magmas whereas magnetite from skarn or skarn-type iron ores is mainly controlled by hydrothermal fluids, which is also supported by the gabbro-linked Zhangmatun iron deposit. Fig. 7 suggests that magnetite from Ji'nan intrusion beneath the Zhangmatun orefield formed through crystallization differentiation of magma, whereas magnetite from both skarn and iron ores is predominantly attributed to the contact metasomatism by hydrothermal fluids. It is notable that several magnetite grains are not shown in the Ni/(Cr + Mn) vs. Ti + V and Ti vs. Ni/Cr diagrams because of their lower concentrations of Ni than the detection limits of LA-ICP-MS.

In general, the primary ore-forming fluids for skarn-type deposits are considered to be mainly magmatic fluids directly derived through exsolution from melts (Wang et al., 1981; Zhang et al., 2014a; Zheng et al., 2007). However, whether magnetite in the skarn-type iron ores was precipitated directly from the primary magmatic fluids or from the evolved ore-forming fluids generated through the involvement of country rocks (including solidified gabbro and carbonate sedimentary rocks) remains debated.

According to Xie et al. (2015), the magnetite in Ji'nan gabbro which formed in the late stage of the magmatic evolution shows an average temperature of 665.5 °C. We take it as the temperature at which exsolution of magmatic fluids occurred. The iron ores for skarn-type iron deposits are recognized to be formed mainly at the temperature range of 600 °C–400 °C (Zhai et al., 2011). Hence,
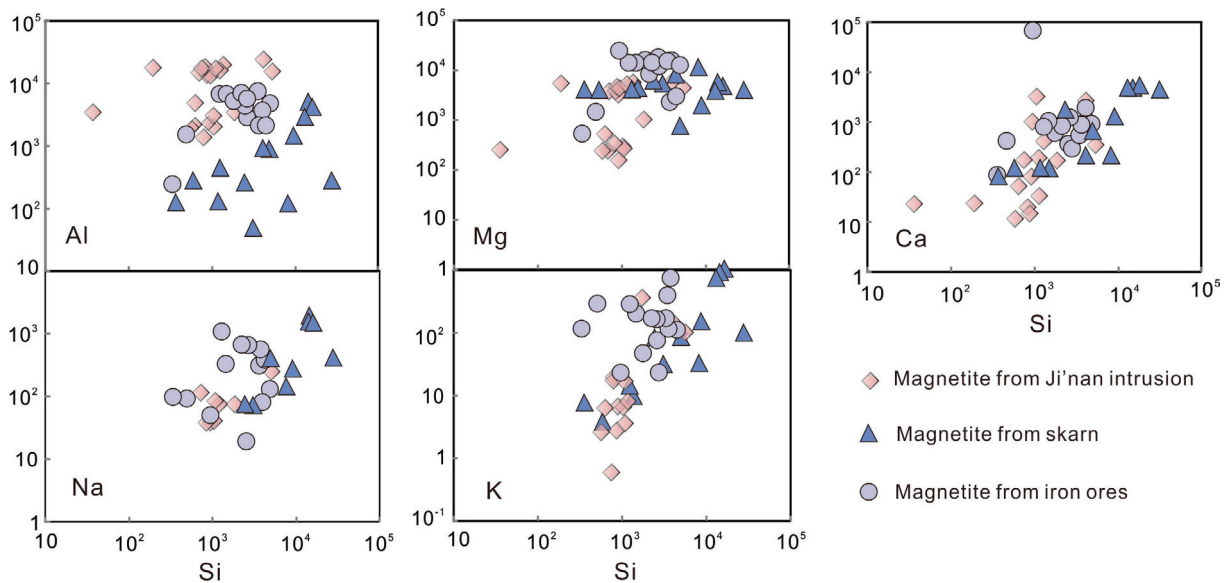
Fig. 5. The characteristics of the trace elements in magnetite (elements in ppm).
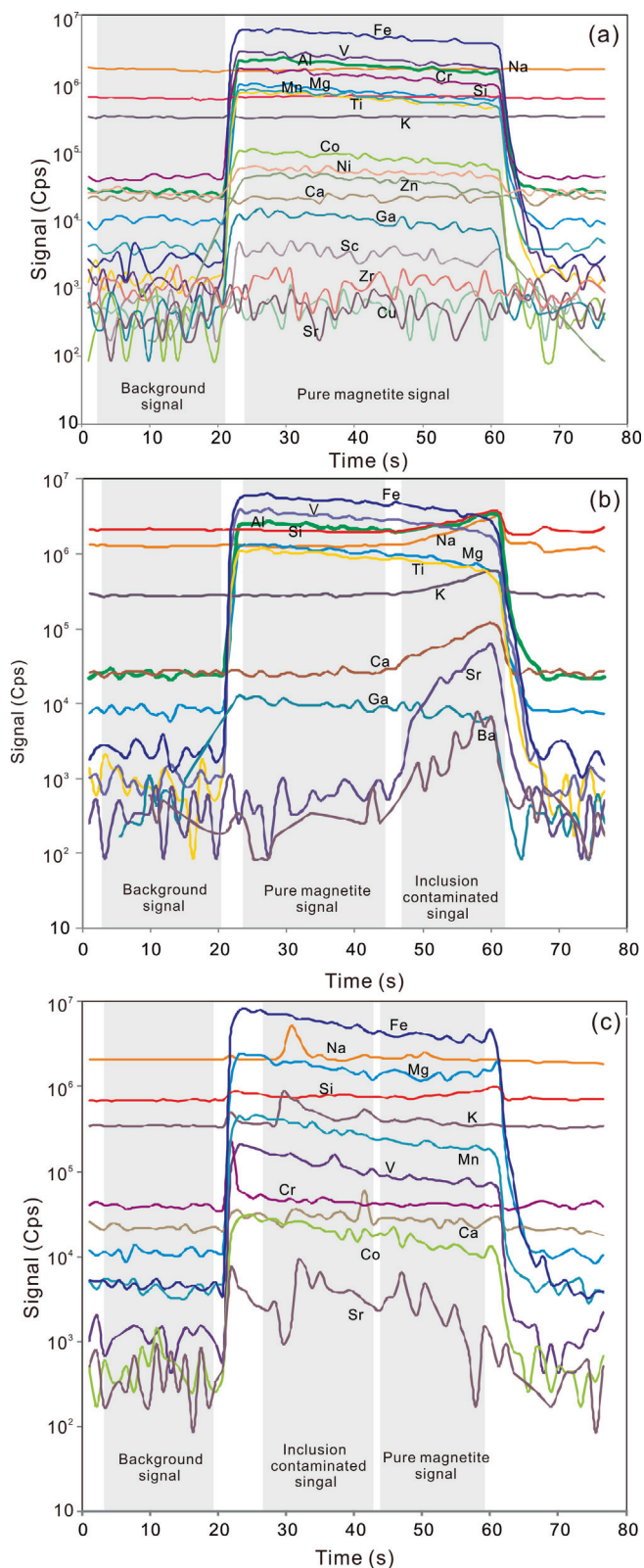
Fig. 6. Time-resolved analytical signals of LA-ICP-MS analyses. (a) Signals of pure magnetite. (b) Signals of representative magnetite with Ca-Mg silicate mineral relict. (c) Signals of representative magnetite with Na, K-rich fluids inclusions.

it is reasonable to take 400 °C as the temperature at which precipitation of magnetite from the ore-forming fluids occurred. The relationship of oxygen isotope fractionation between minerals
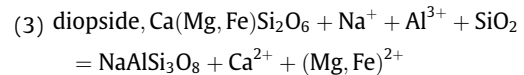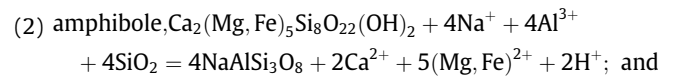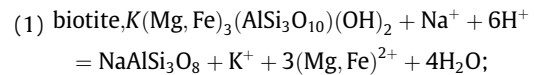
and water at temperature ranging from 0 to 1200 °C (Zheng, 1991, 1993; Zheng et al., 2000), is expressed as

$$10^3 \ln\alpha_{(\text{mineral,water})} = A \times 10^6/T^2 + B \times 10^3/T + C$$

For the diopside-water in equilibrium, the A, B and C in this equation are equal to 3.92, −8.43 and 2.40, respectively, whereas for the magnetite-water in equilibrium, the A, B and C are equal to 2.88, −11.36 and 2.89, respectively (Zheng et al., 2000). As reported by Xie et al. (2015), the diopside in the Ji'nan gabbro shows average $\delta^{18}O_{\text{V-SMOW}}$ of 6.95‰, and the $\delta^{18}O_{\text{V-SMOW}}$ of corresponding water is calculated to be 8.37‰ at 665.5 °C. However, the calculated $\delta^{18}O_{\text{V-SMOW}}$ of water in equilibrium with magnetite ($\delta^{18}O_{\text{V-SMOW}}$ = 3.0‰), in Ji'nan gabbro is 10.68‰, indicating that the diopside and magnetite in the gabbro are not in equilibrium. Considering that the closure temperature of diopside is about 200 °C higher than that of magnetite at the same cooling rate (Guo et al., 2000), we estimate the $\delta^{18}O_{\text{V-SMOW}}$ of water to be about 8.37‰ when the primary magmatic fluids were separated from the gabbroic melts. Besides, as listed in Table 5, the magnetite grains from iron ores (except for the sample of JN-7) show much higher $\delta^{18}O_{\text{V-SMOW}}$ values than those of magmatic magnetite, with the lowest value of 4.3‰. Whether the closure temperature of magnetite precipitated from the ore-forming fluids is higher or lower than 400 °C, the $\delta^{18}O_{\text{V-SMOW}}$ value of the corresponding water is calculated to be equal to or higher than 11.81‰.

Fluid-rock reaction in the retrograde stage may lower the ^{18}O of the hydrothermal fluids. However, in the mineralization system, based on the above discussion, both the $\delta^{18}O_{\text{V-SMOW}}$ values of magnetite and the corresponding water in the final ore-forming fluids were significantly elevated, which suggests that the hydrothermal system was not a closed one, and that the ore-forming fluids were not the primary unreacted magmatic fluids. Oxygen exchange might have taken place between the ore-forming fluids and the ^{18}O-rich carbonate country rocks under relatively high temperatures (>350 °C) (Zheng et al., 2000) which resulted in elevated ^{18}O contents in both hydrothermal fluids and magnetite. In other words, magnetite in the iron ores was predominantly precipitated from evolved ore-forming fluids formed through the reaction between country rocks and the primary magmatic fluids exsolved from the gabbroic melts.

5.3. Implications for iron mineralization

5.3.1. Mechanism of iron concentration

Several models have been proposed for the source of iron in skarn-type deposits related to mafic intrusions, such as: (1) recycling of pre-existing ore deposits (e.g., Johnson et al., 1990; Wang et al., 1981), (2) leaching from sedimentary country rocks (Rose et al., 1985), (3) leaching from associated solidified igneous rocks (e.g., Feng, 1998; Zheng et al., 2007), or (4) exsolution of Fe-rich magmatic fluids from melts during magmatic evolution (e.g., Shimazaki, 1980).

Since there are no pre-existing ore deposits which can supply enough iron found in and/or near the Zhangmatun orefield and that the country rocks in the orefield are predominantly the middle-Ordovician limestone which contains very low iron concentration, it is unlikely that the enrichment of iron resulted from leaching from the pre-existing ore deposits or sedimentary rocks. Moreover, as seen in Fig. 4, in the primitive mantle normalized spider-gram and the chondrite-normalized REE patterns, the magnetite grains from the Ji'nan intrusion, skarn rocks and iron ores show similar patterns, indicating that they may have a common iron source. Considering that the iron in magnetite from the Ji'nan
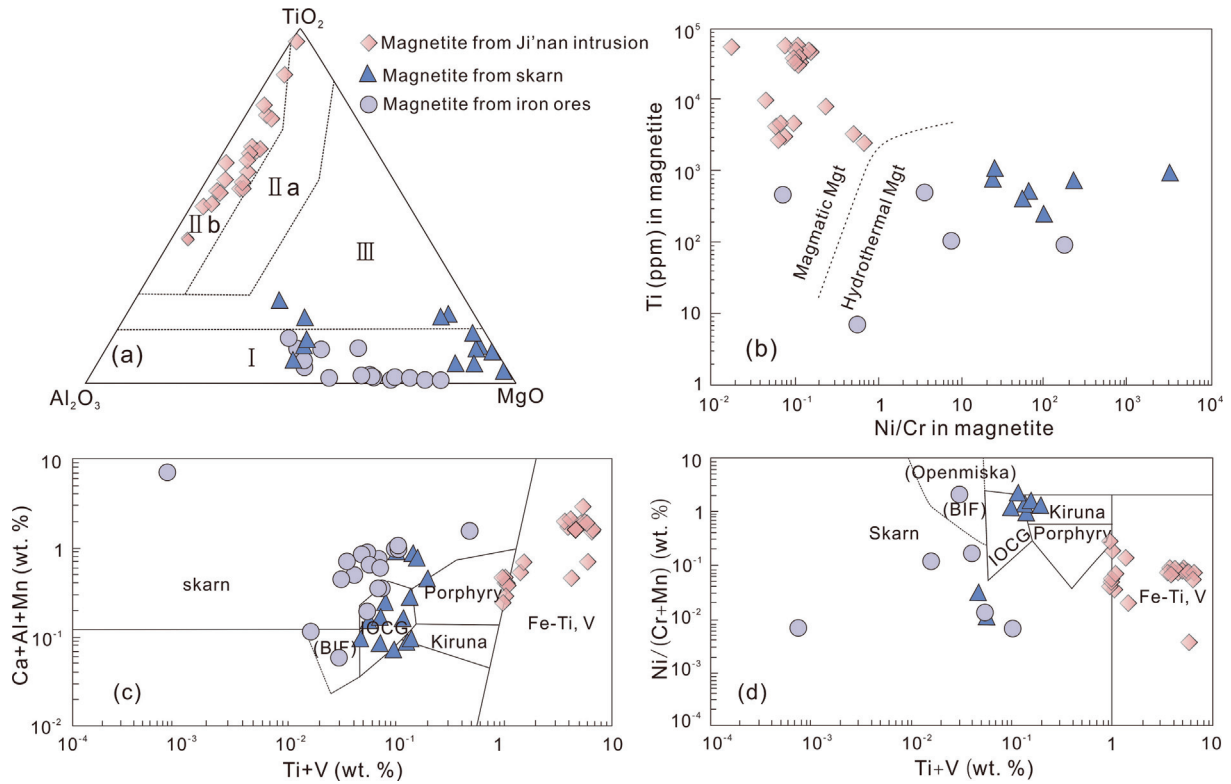
Fig. 7. (a) Plots of TiO_2-Al_2O_3-MgO in magnetite, I-magnetite in sedimentary/metamorphic or skarn deposit, II-magnetite in ultrabasic-basic-intermediate rock, III-magnetite in acid-alkaline rock (after Chen et al. (1987)), (b) Plots of Ca + Al + Mn vs. Ti + V (ppm) in magnetite, (c) Plots of Ni/(Cr + Mn) vs. Ti + V (ppm) ((c)) for LA-ICP-MS data of magnetite from different rocks ((b) and (c) adapted from Dupuis and Beaudoin (2011)), and (d) Plots of Ti (ppm) versus Ni/Cr ratios in magnetite (after Dare et al. (2014)).

intrusion was derived from a mafic parental magma, we infer that iron from the other two rocks are also associated with coeval magmatism involving the emplacement and solidification of gabbroic rocks.

If iron concentration for the Zhangmatun iron deposit is predominantly derived from exsolution of Fe-rich magmatic fluids from a basaltic melt, many dark-colored and Fe-rich fluid inclusions should be observed under microscope. However, neither the ore-related igneous rocks, nor the skarn rocks exhibit such evidence. Additionally, as discussed above, the precipitation of magnetite in iron ores did not occur from the primary magmatic fluids, but was controlled by modified ore-forming fluids with involvement of country rocks in the late stage of hydrothermal evolution. Moreover, previous studies have demonstrated that meteoric water is commonly incorporated into the magmatic fluids in the late stage of hydrothermal activity (Zhang et al., 2014b), which may dilute the iron concentration in fluids if there is no additional supply of iron by country rocks (such as the solidified gabbro). Hence, although we cannot rule out the possibility of magmatic fluids as the iron source, we infer that it is not the dominant source.

Iron concentrated by leaching from the solidified intrusion is one of the popular models applied to many mineralizing districts, based on the extensive albitization that has been regarded as important signs for exploration of potential deposits (Zheng et al., 2007). In the Zhangmatun orefield, albitization is also common in the ore-related gabbro. Most of the biotite and amphibole were replaced by diopside and albite (Fig. 2e–g), and the diopside was also replaced by albite (Fig. 2c). The corresponding reactions (role of Fe^{3+} not shown in these equations) are as below:

(1) biotite, $K(Mg, Fe)_3(AlSi_3O_{10})(OH)_2 + Na^+ + 6H^+$
$$= NaAlSi_3O_8 + K^+ + 3(Mg, Fe)^{2+} + 4H_2O;$$

(2) amphibole, $Ca_2(Mg, Fe)_5Si_8O_{22}(OH)_2 + 4Na^+ + 4Al^{3+}$
$$+ 4SiO_2 = 4NaAlSi_3O_8 + 2Ca^{2+} + 5(Mg, Fe)^{2+} + 2H^+;$$ and

(3) diopside, $Ca(Mg, Fe)Si_2O_6 + Na^+ + Al^{3+} + SiO_2$
$$= NaAlSi_3O_8 + Ca^{2+} + (Mg, Fe)^{2+}$$

As shown by the above equations, albitization of the gabbro beneath the Zhangmatun orefield can release much iron in the form of Fe^{2+} into the ore-forming fluids. Meanwhile, the decreasing FeO^T contents of biotite, amphibole, diopside and albite can also demonstrate that much iron has been lost during the albite alteration. The EMPA data show the average FeO^T contents of 15.85 wt% for biotite in the albitized gabbro, 13.29 wt% for amphibole (Table 1), 5.78 wt% for diopside and 0.24 wt% for albite (Xie et al., 2015). Moreover, the newly formed magnetite and pre-existing magmatic magnetite were dissolved from the strongly altered gabbro, resulting in a decrease in the contents of magnetite from 3.0 vol% in fresh gabbro to ∼0.0 vol% in most strongly altered gabbro, and the corresponding FeO^T contents in the whole rocks decreases from 11.5 wt% to 2.87 wt% (Xie et al., 2015). This feature indicates that much iron was added into ore-forming fluids through leaching from the Fe-rich minerals in solidified gabbro during the albitization process.

To evaluate the possible role of leaching in the Zhangmatun iron mineralization, we assume with that the solidified gabbro is the

main iron source for the Zhangmatun deposit. Considering that the average FeO^T content of fresh gabbro is 8.88 wt% whereas the average FeO^T content of the most strongly altered gabbro in the orefield is 3.57 wt% (Xie et al., 2015), we can roughly estimate that as much as 5.31 wt% FeO^T has been leached out from the solidified intrusion and passed into the ore-forming fluids. Based on the iron ore reserve of 20.74 Mt and the average TFe grade of ~52.55%, the mass of altered gabbro is expected to be 263.9 Mt. Assuming the density of the altered gabbro as 2.7 g/cm^3, the volume of the altered gabbro is calculated to be $9.78 * 10^4 m^3$, less than the actual volume of altered gabbro beneath the Zhangmatun orefield and negligibly minor relative to the total volume of the Ji'nan gabbro. Therefore, iron leached out of the Ji'nan gabbro during albitization is believed to be capable of supplying enough Fe required for the formation of the Zhangmatun iron deposit.

5.3.2. Physicochemical conditions of iron mineralization

The compositional variability of magnetite is affected by several factors including temperature, fluid composition-element availability, oxygen (and sulfur) fugacity, host rock buffering and intrinsic crystallographic controls such as ionic radius and charge balance (Nadoll et al., 2014). According to the previous studies on the fluid inclusions and hydrogen-oxygen isotopes, the ore-forming fluid in the early stage of mineralization for skarn-type iron deposit is predominantly composed of weak alkaline magmatic fluid with high temperature which is mainly derived from exsolution from the corresponding melt in the late stage of magmatic evolution (Zhang et al., 2012, 2014a; Hong et al., 2012; Fan et al., 2012). The primary magmatic hydrothermal fluid is recognized as the foundation of the formation of skarn-type deposits (Zheng et al., 2007), and is also the main media for the extraction, migration and precipitation of metal (iron) elements.

Formation of the Zhangmatun iron deposit has been demonstrated to be a dynamic process, and environmental conditions of the ore-forming fluids significantly varied with time, which can be recorded in magnetite. The geochemical variations exhibited by hydrothermal magnetite (i.e., magnetite from skarn and iron ores) and the much higher $\delta^{18}O_{V\text{-SMOW}}$ values (4.3–6.4‰) of magnetite from iron ores than that from intrusion demonstrate that geochemical compositions, temperature, and oxygen fugacity of ore-forming fluids have changed during the evolution of the hydrothermal fluid, relative to the primary magmatic fluid that exsolved from the gabbroic melt.

The composition of hydrothermal fluids exerts a first order control on the minor and trace element concentrations in hydrothermal magnetite. The enrichment of Ti and Al in magnetite from skarn and iron ores indicates relatively high concentrations of these two elements in the ore-forming fluids. As demonstrated from experimental studies, Ti and Al are immobile and are typically not detected in hydrothermal fluids at sub-magmatic temperatures (Nadoll and Koenig, 2011; Verlaguet et al., 2006). Therefore the Ti and Al, together with the Ti-dependent elements such as Au, Ag and Cu (Simon et al., 2008), incorporated in the hydrothermal magnetite in the Zhangmatun deposit might not have been derived from leaching, but from the exsolution of fluids from melt at magmatic temperature. Furthermore, Ti and Al concentrations in magnetite are directly controlled by temperature (Nielsen et al., 1994), and the higher concentrations indicate higher temperatures. The decrease in concentrations of these elements in magnetite suggests a decreasing temperature of ore-forming fluids during the mineralization.

The incorporation of Ni, a typical siderophile element in magnetite is restricted to very low oxygen fugacity condition because it is otherwise more likely to form pentlandite (Drabek, 1982). As seen in Table 2, the Ni concentration in all the analyzed samples of magmatic magnetite are above the detection limits of LA-ICP-MS, whereas several magnetite grains from skarn and most magnetite from iron ores show Ni concentrations below detection limit, suggesting that the oxygen fugacity of ore-forming fluids increased with the evolving fluids. Additionally, concentrations of Cr and V in magnetite are also controlled by oxygen fugacity (Klemme et al., 2006; Righter et al., 2006). Vanadium is usually preferentially incorporated into the magnetite structure at low oxygen fugacity and becomes incompatible at high oxygen fugacity due to its 5+ oxidation state (Bordage et al., 2011; Toplis and Corgne, 2002). The decreasing concentrations of Cr and V in the hydrothermal magnetite further demonstrate that the oxygen fugacity became higher as the ore-forming fluids evolved. Besides, as albitization of gabbro is common in the Zhangmatun orefield, geochemical composition of the genetically-linked hydrothermal fluids significantly varies, including elevated iron concentration, decreased Na concentration and the transformation of the fluids from weakly alkaline to acidic (Wang et al., 1981; Zhang et al., 2014a).

Finally, as the Fe-rich ore-forming fluids migrated into the cold and brittle carbonate country rocks, the Ca concentration increased (Table 3 and Fig. 5), with the Ordovician Majiagou limestones buffering the conditions to decreasing temperature and pressure. Meanwhile, the oxygen fugacity was significantly increased through the O isotopic exchange between fluids and the ^{18}O-rich carbonate country rocks. During this process, large volumes of H^+ cations in ore-forming fluids were consumed, which resulted in the pH increase.

The changes in hydrothermal fluids resulted in an increase in the iron concentration in early stage and/or decreasing the iron solubility in late stage of hydrothermal fluids evolution (Simon et al., 2004). As a result of the processes above, large volumes of magnetite precipitated from the Fe-rich ore-forming fluids, leading to the formation of the massive iron ores of the Zhangmatun skarn-type iron deposit.

6. Conclusions

Magnetite grains in the Ji'nan gabbro, skarn, and iron ores show similar primary mantle normalized spider-gram and chondrite-normalized REE patterns, suggesting that Fe in them might have been derived from a common iron source, inferred as a mafic parental magma. In the time-resolved analytical signals of LA-ICP-MS, the abnormal signals of incompatible elements of Si, Ca and Mg are attributed to the sub-micro-scale silicate mineral inclusions in magnetite. The abnormal signals of Na, K are attributed to the micro- to nano-scale salt-bearing fluid inclusions in magnetite. Additionally, in the magmatic-hydrothermal system, the $\delta^{18}O_{V\text{-SMOW}}$ values of the final ore-forming fluids were much higher than those of the primary magmatic fluids, indicating that oxygen isotopic exchange between the hydrothermal fluids and ^{18}O-rich carbonate country rocks occurred at a relatively high temperature before the precipitation of magnetite.

The iron in the ore deposit was derived mainly through leaching from the solidified ore-related gabbro, during the contact metasomatism by hydrothermal fluids. The variations in geochemical compositions, temperature, pressure and oxygen fugacity of ore-forming fluids and the fluid/rock interaction exerted significant control on the precipitation of magnetite from fluids, leading to the formation of the Zhangmatun skarn-type iron deposit.

References

Armstrong, J.T., 1995. CITZAF a package of correction programs for the quantitative electron microbeam X-ray analysis of thick polished materials, thin films and particles. Microbeam Anal. 4, 117–200.

Beaudoin, G., Dupuis, C., Gosselin, P., Jébrak, M., 2007. Mineral chemistry of iron oxides: application to mineral exploration. In: Andrew, C.J. (Ed.), Ninth Biennial SGA Meeting. SGA, Dublin, pp. 497–500.

Bordage, A., Balan, E., Villiers, J.R., Cromarty, R., Juhin, A., Carvallo, C., et al., 2011. V oxidation state in Fe-Ti oxides by high-energy resolution fluorescence-detected X-ray absorption spectroscopy. Phys. Chem. Miner. 38, 449–458.

Bowles, J.F.W., Howie, R.A., Vaughan, D.J., Zussman, J., 2011. Rock-Forming Minerals (Volume 5A): Non-Silicates – Oxides, Hydroxides and Sulphides. The Geological Society, London.

Bragg, W.H., 1915. The structure of the spinel group of crystals. Phil. Mag. 30, 305–315.

Carew, M.J., 2004. Controls on Cu-Au Mineralisation and Fe Oxide Metasomatism in the Eastern Fold Belt, N.W. Queensland, Australia (Unpublished Ph.D. thesis). James Cook University.

Chen, G.Y., Sun, D.S., Yin, H.A., 1987. Genetic and Prospecting Mineralogy. Chongqing Publishing Group, Chongqing, pp. 1–29 (in Chinese).

Chen, W., Zhou, M.F., Li, X.C., Gao, J.F., Hou, K.J., 2015. In-situ LA-ICP-MS trace elemental analyses of magnetite: Cu-(Au, Fe) deposits in the Khetri copper belt in Rajasthan Province, NW India. Ore Geol. Rev. 65, 929–939.

Dare, S.A.S., Barnes, S.J., Beaudoin, G., 2012. Variation in trace element content of magnetite crystallized from a fractionating sulfide liquid, Sudbury, Canada: implications for provenance discrimination. Geochim. Cosmochim. Acta 88, 27–50.

Dare, S.A.S., Barnes, S.J., Beaudoin, G., Méric, J., Boutroy, E., Potvin-Doucet, C., 2014. Trace elements in magnetite as petrogenetic indicators. Mineral Deposits 49, 785–796.

Drabek, M., 1982. The system Fe-Mo-S-O and its geologic application. Econ. Geol. 77, 1053–1056.

Duan, C., Li, Y.H., Yuan, S.D., Hu, M.Y., Zhao, L.H., Chen, X.D., Zhang, C., Liu, G.L., 2012. Geochemical characteristics of magnetite from Washan iron deposit in Ningwu ore district and its constraints on ore-forming. Acta Petrol. Sin. 28 (1), 243–257 (in Chinese with English abstract).

Dupuis, C., Beaudoin, G., 2011. Discriminant diagrams for iron oxide trace element fingerprinting of mineral deposit types. Miner. Deposita 46, 319–335.

Eugster, H.P., Chou, I.M., 1979. A model for the deposition of Cornwall-type magnetite deposits. Econ. Geol. 74, 763–774.

Fan, Y., Zhou, T.F., Hao, L., Yuan, F., Zhang, L.J., Wang, W.C., 2012. Ore-forming fluid characteristic of Nihe iron deposit in Lu-Zong basin, Anhui Province and its significance to ore genesis. Acta Petrol. Sin. 28 (10), 3113–3124.

Feng, Z.Y., 1998. Comparison of iron skarn generating intrusions with barren intrusions in Southern Taihang Mountain, China. Geosciences 1, 467–476 (in Chinese with English abstract).

Fleet, M., 1981. The structure of magnetite. Acta Crystallogr. B 37, 917–920.

Fleet, M., 1986. The structure of magnetite: symmetry of cubic spinels. J. Solid State Chem. 62 (1), 75–82.

Gao, J.F., Zhou, M.F., Lightfoot, P.C., Wang, C.Y., Qi, L., Sun, M., 2013. Sulfide saturation and magma emplacement in the formation of the Permian Huangshandong Ni-Cu Sulfide Deposit, Xinjiang, Northwestern China. Econ. Geol. 108, 1833–1848.

Gosselin, P., Beaudoin, G., Jébrak, M., 2006. Application of the Geochemical Signature of Iron oxides to Mineral Exploration: GAC-MAC Annual Meeting Prog Abs 31: CD-ROM.

Grigsby, J.D., 1990. Detrital magnetite as a provenance indicator. J. Sediment. Res. 60 (6), 940–951.

Guo, J.B., Qian, Y.Q., Huang, Y.S., 2000. Oxygen isotope kinetics of skarn deposit in Anqing. Volcanol. Mineral Resour. 21, 23–29.

Han, Y.W., Ma, Z.D., Zhang, H.F., Zhang, B.R., Li, F.L., Gao, S., Bao, Z.Y., 2002. Geochemistry. Geology Publishing House, Beijing, p. p. 33.

Hong, W., Zhang, Z.H., Li, F.M., Liu, X.Z., 2012. Stable isotopic characteristics of Chagangnuoer iron deposit in western Tianshan, Xinjiang and its geological significance. Rock Mineral Anal. 31 (6), 1077–1087.

Hou, T., Zhang, Z., Santosh, M., John, E., Wang, M., 2013. The Cihai diabase in the Beishan region, NW China: isotope geochronology, geochemistry and implications for Cornwall-style iron mineralization. J. Asian Earth Sci. 70–71, 231–249.

Hu, H., Duan, Z., Luo, Y., Li, J.W., 2014. Trace element systematics of magnetite from the Chengchao iron deposit in the Daye district: a laser ablation ICP-MS study and insights into ore genesis. Acta Petrol. Sin. 30 (5), 1292–1306.

Huang, X.W., Zhou, M.F., Qi, L., Gao, J.F., Wang, Y.W., 2013. Re-Os isotopic ages of pyrite and chemical composition of magnetite from the Cihai magmatic-hydrothermal Fe deposit, NW China. Miner. Deposita 48, 925–946.

Lapham, D.M., Gray, C., 1973. Geology and Origin of the Triassic Magnetite Deposits and Diabase at Cornwall, Pennsylvania. Pennsylvania Geological Survey Bulletin M56. 343 p.

Jin, Z.L., Zhang, Z.C., Huang, H., Santosh, M., Hou, T., 2014. Geochronology and geochemistry of the Airikenqiken granite, Central Tianshan Terrane, Xinjiang, China: implications for petrogenesis and continental growth. Int. Geol. Rev. 56 (7), 801–822.

Johnson, C.A., Rye, D.M., Skinner, B.J., 1990. Petrology and stable isotope geochemistry of the metamorphosed zinc-iron-manganese deposit at Sterling Hill, New Jersey. Econ. Geol. 85, 1133–1161.

Klemme, S., Günther, D., Hametner, K., Prowatke, S., Zack, T., 2006. The partitioning of trace elements between ilmenite, ulvospinel, armalcolite and silicate melts with implications for the early differentiation of the moon. Chem. Geol. 234, 251–263.

Li, Y., Hou, K., Wan, D., Zhang, Z., Yue, G., 2014. Precambrian banded iron formations in the North China Craton: silicon and oxygen isotopes and genetic implications. Ore Geol. Rev. 57, 299–307.

Liu, S., Hu, R., Gao, S., Feng, C., Qi, L., Zhong, H., Xiao, T., Qi, Y., Wang, T., Coulson, I.M., 2008. Zircon U-Pb geochronology and major, trace elemental and Sr–Nd–Pb isotopic geochemistry of mafic dykes in western Shandong Province, east China: constrains on their petrogenesis and geodynamic significance. Chem. Geol. 255, 329–345.

Meinert, L.D., 1992. Skarns and skarn deposits. Geosci. Canada 19 (4), 145–162.

Meinert, L.D., Dipple, G.M., Stefan, N., 2005. World skarn deposits. Soc. Econ. Geol. 100, 299–336.

Nadoll, P., Angerer, T., Mauk, J., French, D., Walshe, J., 2014. The chemistry of hydrothermal magnetite: a review. Ore Geol. Rev. 61, 1–32.

Nadoll, P., Koenig, A.E., 2011. LA-ICP-MS of magnetite: methods and reference materials. J. Anal. At. Spectrom. 26, 1872–1877.

Nielsen, R.L., Forsythe, L.M., Gallahan, W.E., Fisk, M.R., 1994. Major- and trace-element magnetite-melt equilibria. Chem. Geol. 117, 167–191.

Qiu, J., Hu, J., Jiang, S., Wang, R., Xu, X., 2005. Mesozoic-Cenozoic mafic magmatism in western Shandong Province and its implication for the Chemical evolution of the mantle. Earth Sci. 30 (6), 646–658 (in Chinese with English abstract).

Ramdohr, P., 1980. The Ore Minerals and Their Intergrowths. Pergamon, New York.

Razjigaeva, N.G., Naumova, V.V., 1992. Trace element composition of detrital magnetite from coastal sediments of Northwestern Japan Sea for provenance study. J. Sediment. Petrol. 62, 802–809.

RGS (Regional Geological Survey) Shandong Province, 1991. Geology of Shandong Province (in Chinese). Geological Publishing House, Beijing.

Righter, K., Sutton, S.R., Newville, M., Le, L., Schwandt, C.S., Uchida, H., et al., 2006. An experimental study of the oxidation state of vanadium in spinel and basaltic melt with implications for the origin of planetary basalt. Am. Mineral. 91, 1643–1656.

Rose, A.W., Herrick, D.C., Deines, P., 1985. An oxygen and sulfur isotope study of skarn-type magnetite deposits of the Cornwall type, Southeastern Pennsylvania. Econ. Geol. 80, 418–443.

Savard, D., Barnes, S.-J., Sunder Raju, P.V., 2010. Accurate LA-ICP-MS calibration for magnetite analysis using multiple reference materials. In: Goldschmidt Conference Abstracts A914.

Scheka, S.A., Platkov, A.V., Vezhosek, A.A., Levashov, G.B., Oktyabrsky, R.A., 1980. The Trace Element Paragenesis of Magnetite. Nauka, Moscow, p. 147.

Shimazaki, H., 1980. Characteristics of skarn deposits and related acid magmatism in Japan. Econ. Geol. 75, 173–183.

Simon, A., Pettke, T., Candela, P., Piccoli, P., Heinrich, C., 2004. Magnetite solubility and iron transport in magmatic-hydrothermal environments. Geochim. Cosmochim. Acta 68 (23), 4905–4914.

Simon, A.C., Candela, P.A., Piccoli, P.M., Mengason, M., Englander, L., 2008. The effect of crystal–melt partitioning on the budgets of Cu, Au, and Ag. Am. Mineral. 93, 1437–1448.

Singoyi, B., Danyushevsky, L., Davidson G., Large R and Zaw K., 2006. Determination of trace elements in magnetites from hydrothermal deposits using the LA ICP-MS technique. Denver, USA: SEG Keystone Conference, CD-ROM.

Song, M., Li, H., 2001. Study on regional geological structural evolution in Shandong Province. Geol. Shandong Province 17 (6), 12–21 (in Chinese with English abstract).

Sun, S., McDonough, W.F., 1989. Chemical and isotopic systematic basalt, implication for mantle composition and processes. Geol. Soc. Spec. Pub. 42, 313–345.

Tang, D.M., Qin, K.Z., Chen, B., Mao, Y.J., Guo, H., Evans, N.J., 2017. Mineral chemistry and genesis of the Permian Cihai and Cinan magnetite deposits, Beishan, NW China. Ore Geol. Rev. 86, 79–99.

Toplis, M., Corgne, A., 2002. An experimental study of element partitioning between magnetite, clinopyroxene and iron-bearing silicate liquids with particular emphasis on vanadium. Contrib. Miner. Petrol. 144, 22–37.

Verlaguet, A., Brunet, F., Goffé, B., Murphy, W.M., 2006. Experimental study and modeling of fluid reaction paths in the quartz–kyanite ± muscovite–water system at 0.7 GPa in the 350–550 °C range: implications for Al selective transfer during metamorphism. Geochim. Cosmochim. Acta 70, 1772–1788.

Wang, Y.L., Ren, F.G., Shi, Y., 1981. Discuss the iron source and origin of the iron ore deposit of Hanxing type. Bull. Tianjin Inst. Geol. Mineral Resour. 3, 1–10 (in Chinese with English abstract).

Wechsler, B.A., Lindsley, D.H., Prewitt, C.T., 1984. Crystal structure and cation distribution in titanomagnetites ($Fe_3-_xTi_xO_4$). Am. Mineral. 69, 754–770.

Xie, Q.H., Zhang, Z.C., Hou, T., Santosh, M., Jin, Z.L., Han, L., Cheng, Z.G., 2015. Petrogenesis of the Zhangmatun gabbro in the Ji'nan complex, North China Craton: Implications for the skarn-type iron mineralization. J. Asian Earth Sci. 113, 1197–1217.

Xu, Y., 2002. Evidence for crustal components in mantle source and constraints on recycling mechanism: pyroxenite xenoliths from Hannuoba, North China. Chem. Geol. 182, 301–322.

Yang, C., Xu, W., Yang, D., Liu, C., Liu, X., Hu, Z., 2005. Chronology of the Jinan gabbro in western Shandong: evidence from LA-ICP-MS zircon U-Pb dating. Acta Geosci. Sin. 26 (4), 321–325 (in Chinese with English abstract).

Yang, Q., Zhao, Z., Zheng, Y., 2012. Slab-mantle interaction in continental subduction channel: geochemical evidence from Mesozoic gabbroic intrusives in southeastern North China. Lithos 155, 442–460.

Yang, S., Wang, Z., Guo, Y., Li, C., Cai, J., 2009. Heavy mineral compositions of the Changjiang (Yangtze River) sediments and their provenance-tracing implication. J. Asian Earth Sci. 35, 56–65.

Yang, S.Y., Li, C.X., Zhu, J.C., 2000. Provenance indicator of chemical fingerprint of magnetite from the Yangtze River and the Yellow River sediments. Geochimica 29 (5), 478–484 (in Chinese with English abstract).

Zhang, X., Zhang, Y., Ji, W., 2007. Fault distribution patterns of the Luxi Block, Shandong, and Mesozoic sedimentary-magmatic-structural evolution sequence. J. Geomech. 13 (2), 163–170 (in Chinese with English abstract).

Zhai, Y., Yao, S., Cai, K., 2011. Mineral Deposits. Geological Publishing House, pp. 96–122.

Zhang, Z.C., Hou, T., Li, H.M., Li, J.W., Zhang, Z.H., Song, X.Y., 2014a. Enrichment mechanism of iron in magmatic-hydrothermal system. Acta Petrol. Sin. 30 (5), 1189–1204.

Zhang, Z.C., Hou, T., Santosh, M., Li, H.M., Li, J.W., Zhang, Z.H., Song, X.Y., Wang, M., 2014b. Spatio-temporal distribution and tectonic settings of the major iron deposits in China: an overview. Ore Geol. Rev. 57, 247–263.

Zhang, Z.H., Hong, W., Jiang, Z.S., Duan, S.G., Wang, Z.H., Li, F.M., Shi, F.P., Zhao, J., Zheng, R.Q., 2012. Geological features, mineralization types and metallogenic setting of Late Paleozoic iron deposits in western Tianshan Mountains of Xinjiang. Mineral Deposit 31 (5), 941–964.

Zhao, W.W., Zhou, M.F., 2014. In-situ LA-ICP-MS trace element analyses of magnetite: the Mesozoic Tengtie skarn Fe deposit in the Nanling Range, South China. Ore Geol. Rev. 65, 872–883.

Zheng, J.H., Mao, J.W., Yang, F.Q., Chai, F.M., Zhu, Y.F., 2017. Mineralogy, fluid inclusions, and isotopes of the Cihai iron deposit, eastern Tianshan, NW China: implication for hydrothermal evolution and genesis of subvolcanic rocks-hosted skarn-type deposits. Ore Geol. Rev. 86, 404–425.

Zheng, J.M., Mao, J.W., Chen, M.H., Li, G.D., Ban, C.Y., 2007. Geological characteristics and metallogenic model of skarn iron deposits in the Handan-Xingtai area, southern Hebei, China. Geol. Bull. China 26, 150–154 (in Chinese with English abstract).

Zheng, Y.F., 1991. Calculation of oxygen isotope fractionation in metal oxide. Geochim. Cosmochim. Acta 55, 2299–2307.

Zheng, Y.F., 1993. Calculation of oxygen isotope fractionation in anhydrous silicate minerals. Geochim. Cosmochim. Acta 57, 1079–1091.

Zheng, Y.F., Xu, B.L., Zhou, G.T., 2000. Geochemical studies of stable isotopes in minerals. Earth Sci. Front. (China University of Geosciences, Beijing) 7 (2), 299–320.